

Solving Coupled Problems of Blood Flow and Coagulation in Moving Domains, I: Numerical Models and Simulations

I. Konshin^{1,2,3,4*}, K. Terekhov^{1,5**}, and Yu. Vassilevski^{1,3,4***}

(Submitted by A. V. Lapin)

¹Marchuk Institute of Numerical Mathematics of the Russian Academy of Sciences,
Moscow, 119333 Russia

²Federal Research Center “Computer Science and Control” of the Russian Academy of Sciences,
Moscow, 119333 Russia

³Moscow Institute of Physics and Technology, Dolgoprudny, Moscow oblast, 141701 Russia

⁴Institute of Computer Sciences and Mathematical Modeling, Sechenov First Moscow State Medical
University, Moscow, 119991 Russia

⁵Sirius University of Science and Technology, Sochi, 354340 Russia

Received September 30, 2024; revised December 9, 2024; accepted December 12, 2024

Abstract—We consider biophysical problems appearing in moving domains: blood flow, two-phase flow of blood with drifting clot, and coagulation process in blood flow. The corresponding mathematical models are given by the incompressible Navier–Stokes equations, the incompressible Navier–Stokes–Cahn–Hilliard equations, and the Navier–Stokes–Brinkman equations with coagulation equations for chemical kinetics and advection–diffusion of blood factors, respectively. We address blood flow problems that may attract interest of clinicians: clot-in-transit and the clot formation in blood streams. The present paper is the first in the series, where we discuss models, computational meshes, discretizations and results of simulations obtained with the fully implicit solution of aforementioned problems and pave the way for the further investigation of the algebraic solvers efficiency in the second paper of the series.

2010 Mathematics Subject Classification: 65F10, 65F08, 65F05, 92C10, 93A30

DOI: 10.1134/S1995080224608567

Keywords and phrases: *blood flow, embolization, coagulation, Navier–Stokes, Navier–Stokes–Cahn–Hilliard, Navier–Stokes–Brinkman, chemical reactions*

1. INTRODUCTION

Medical procedures often require risk assessment. The latter is best performed in silico using computational fluid dynamics tools due to their non-invasive nature [2, 8, 12, 37, 39, 43]. In this work, we are concerned with the blood flow and blood vessel embolization due to clot detachment [25, 34] or clot growth [1, 4, 5, 22, 44]. The resulting systems of differential equations are combinations of either the Navier–Stokes equations coupled with Cahn–Hilliard equations or the Navier–Stokes equations with the Brinkman terms coupled with coagulation equations for chemical kinetics and advection–diffusion of blood factors. Additional difficulties arise from posing the problems in moving domains. A discretization of the PDEs in moving domains is built in the framework of four-dimensional finite-volume method [32] that is a generalization of three-dimensional finite-volume collocated methods [28, 29, 31, 38]. Such applications require implicit discretizations [21] and the arising nonlinear systems of algebraic equations are difficult to solve [7, 14]. For instance, the Cahn–Hilliard equations are of biharmonic type, whereas equations for chemical kinetics are extremely stiff.

*E-mail: igor.konshin@gmail.com

**E-mail: terekhov@inm.ras.ru

***E-mail: yuri.vassilevski@gmail.com

The present paper is the first in the series where we discuss underlying mathematical models, computational domains and meshes, discretization methods and report the results of simulations which may attract interest of clinicians. In particular, we address scenarios of the clot-in-transit [23] and the clot formation in the ventricle due to tissue inflammation following acute myocardial infarction [26]. The scale of the problem requires the use of supercomputing resources whereby we use up to 50 nodes of the “Lomonosov-2” supercomputer [40]. The second paper in the series [17] will address the iterative solution of arising algebraic systems, parallel performance of the simulations, as well as contribution of all modeling stages to the computational time.

The article is organized as follows. In Section 2, we describe mathematical models considered in this work. Computational domains and computational meshes are discussed in Section 3. Discretization methods for the coupled systems of partial differential equations forming the models are presented in Section 4. Section 5 describes problem setups and results of simulations. Finally, the concluding remarks are given in Section 6.

2. MATHEMATICAL MODELS

2.1. Navier–Stokes Equations For Incompressible Fluid Flow

Flows of incompressible fluid are described by the Navier–Stokes equations

$$\begin{aligned} \partial_t \mathbf{u} + \operatorname{div} (\mathbf{u}\mathbf{u}^T - \nu_b (\nabla \mathbf{u} + \nabla \mathbf{u}^T) + p\mathbb{I}) &= \mathbf{0}, \\ \operatorname{div} (\mathbf{u}) &= 0, \end{aligned} \quad (1)$$

where $\mathbf{u} = [u, v, w]^T$ is the velocity vector, p is the pressure, and $\nu_b = \mu_b/\rho_b$ is the kinematic viscosity of the fluid (blood). System (1) is supplemented with the general type of boundary conditions

$$\boldsymbol{\alpha}\mathbf{u} + \boldsymbol{\beta} (\nu_b (\nabla \mathbf{u} + \nabla \mathbf{u}^T) - p\mathbb{I}) \mathbf{n} = \boldsymbol{\gamma} \quad (2)$$

at $\partial\Omega$, where $\boldsymbol{\alpha} = \alpha_{\parallel}\mathbb{I} + (\alpha_{\perp} - \alpha_{\parallel}) \mathbf{nn}^T$ and $\boldsymbol{\beta} = \beta_{\parallel}\mathbb{I} + (\beta_{\perp} - \beta_{\parallel}) \mathbf{nn}^T$ are second-order tensorial parameters fixing velocity and traction at the boundary and $\boldsymbol{\gamma}$ is the right-hand side vector. The parameters may have different values at different parts of $\partial\Omega$. The initial condition initializes the velocity field. The units are: for length [mm], for time [s], for velocity [mm · s⁻¹]. The kinematic viscosity of fluid in all the tests is $\nu_b = 4$ [mm² · s⁻¹] (conventional viscosity of blood). The nonlinear rheology of the blood [3] is ignored in this work.

2.2. Navier–Stokes–Cahn–Hilliard Equations For Two-Phase Incompressible Fluid Flow

Flows of drifting clots in blood streams may be represented by two-phase incompressible fluid flow that is described by the Navier–Stokes–Cahn–Hilliard equations [6, 13, 20]:

$$\begin{aligned} \partial_t \mathbf{u} + \operatorname{div} (\mathbf{u}\mathbf{u}^T - \nu(\varphi) (\nabla \mathbf{u} + \nabla \mathbf{u}^T) + p\mathbb{I}) &= \mathbf{0}, \\ \operatorname{div} (\mathbf{u}) &= 0, \\ \partial_t \varphi + \operatorname{div} (\varphi \mathbf{u} - \epsilon M(\varphi) \nabla \mu) &= 0, \\ \mu &= -\operatorname{div} (\epsilon \nabla \varphi) + \frac{\varphi^3 - \varphi}{\epsilon}, \end{aligned} \quad (3)$$

where $\varphi \in [-1; 1]$ is the non-dimensional phase indicator function and μ is the chemical potential [mm⁻¹]. The blood phase corresponds to $\varphi = -1$, and the clot phase corresponds to $\varphi = 1$. In addition to (2) equations (3) are supplemented by boundary conditions on $\partial\Omega$ $\alpha_{\varphi}\varphi + \beta_{\varphi} \mathbf{n} \cdot \nabla \varphi = \gamma_{\varphi}$ for the phase indicator function and $\mathbf{n} \cdot \nabla \mu = 0$ for the chemical potential. The kinematic viscosity function $\nu(\varphi) = \nu_b \frac{1-\varphi}{2} + \nu_c \frac{1+\varphi}{2}$ is based on the blood kinematic viscosity $\nu_b = 4$ [mm² · s⁻¹] and the clot kinematic viscosity $\nu_c = 50$ [mm² · s⁻¹] [24], the nonlinear mobility function is given by $M(\varphi) = M_0 \sqrt{(1-\varphi)^2 + \epsilon^2}$ with $M_0 = 1$ [mm² · s⁻¹], where phase interface thickness $\epsilon = 0.1$ [mm]. The initial condition initializes the velocity field and the phase indicator function.

2.3. Navier–Stokes–Brinkman Equations For Incompressible Reactive Fluid Flow

Clot growth in a blood stream is described by the Navier–Stokes equations with the Brinkman term and coagulation equations for chemical kinetics and advection–diffusion of blood factors [4, 5, 7]

$$\begin{aligned}
 \partial_t \mathbf{u} + \operatorname{div}(\mathbf{u}\mathbf{u}^T - \nu_b(\nabla \mathbf{u} + \nabla \mathbf{u}^T) + p\mathbb{I}) + \frac{\nu_b}{K}\mathbf{u} &= \mathbf{0}, \\
 \operatorname{div}(\mathbf{u}) &= 0, \\
 \partial_t P + \operatorname{div}(\mathbf{u}P - D\nabla P) &= -(k_1\phi_a + k_2B + k_3T + k_4T^2 + k_5T^3)P, \\
 \partial_t T + \operatorname{div}(\mathbf{u}T - D\nabla T) &= (k_1\phi_a + k_2B + k_3T + k_4T^2 + k_5T^3)P - k_6AT, \\
 \partial_t B + \operatorname{div}(\mathbf{u}B - D\nabla B) &= (k_7\phi_a + k_8T)(B^0 - B) - k_9AB, \\
 \partial_t A + \operatorname{div}(\mathbf{u}A - D\nabla A) &= -k_6AT - k_9AB, \\
 \partial_t G + \operatorname{div}(\mathbf{u}G - D\nabla G) &= -k_{10}TG(k_{11} + G)^{-1}, \\
 \partial_t F + \operatorname{div}(\mathbf{u}F - D\nabla F) &= k_{10}TG(k_{11} + G)^{-1} - k_{12}F, \\
 \partial\phi_f + \operatorname{div}(k(\phi_f, \phi_a)(\mathbf{u}\phi_f - D_p\nabla\phi_f)) &= -(k_{13}T + k_{14}\phi_a)\phi_f, \\
 \partial\phi_a + \operatorname{div}(k(\phi_f, \phi_a)(\mathbf{u}\phi_a - D_p\nabla\phi_a)) &= (k_{13}T + k_{14}\phi_a)\phi_f, \\
 \partial_t M &= k_{12}F,
 \end{aligned} \tag{4}$$

with concentrations of prothrombin P or factor FII nM, thrombin T or factor FIIa nM, tissue factors B or sum of factors IX and X nM, antithrombin A or factor ATIII nM, fibrinogen G or factor FI nM, fibrin F or factor FIa nM, fibrin polymer M nM, platelets ϕ_f in the flow [10^3 mm^{-3}], platelets ϕ_a in the clot [10^3 mm^{-3}].

Here the clot permeability [45] is calculated by

$$\frac{1}{K} = \frac{16}{r^2}S^{3/2}(1 + 56S^3)\frac{\phi_f + \phi_a}{\phi_f - \phi_a}, \tag{5}$$

where $S = \min(4900, M)/7000$ is the saturation of the media by fibrin polymer [4], $r = 6 \times 10^{-4}$ mm is the fiber radius [4, 45]. The flow of the platelets is constrained by

$$k(\phi_f, \phi_a) = \tanh\left(\pi\frac{\phi_{\max} - \phi_f - \phi_a}{\phi_{\max}}\right), \tag{6}$$

where $\phi_{\max} = 400$ [10^3 mm^{-3}], for details refer to [19]. The coefficients of blood coagulation chemical kinetics are collected in Table 1. The remaining constants are [4]: $B^0 = 200$ nM is the default concentration of tissue factors, $D = 5 \times 10^{-5} \text{ mm}^2 \text{ s}^{-1}$ is the diffusion coefficient for the blood factors, $D_p = 2.5 \times 10^{-5} \text{ mm}^2 \text{ s}^{-1}$ is the diffusion coefficient for the platelets.

System (4) is closed with the boundary conditions (2) and $\alpha_c c + \beta_c D\mathbf{n} \cdot \nabla c = \gamma_c$, where $c \in \{P, T, B, A, G, F, \phi_f, \phi_a\}$. The parameters may have different values at different parts of $\partial\Omega$. The clot growth is initiated by the damage of the endothelium, which is described by the nonlinear boundary condition for the tissue factor $\mathbf{n} \cdot \nabla B = \frac{k_{15}(B^0 - B)}{1 + k_{16}(B^0 - B)}$, where $k_{15} = 7.7 \times 10^4 \text{ nM}^{-1} \text{ s}$ and $k_{16} = 2.25 \times 10^{-1} \text{ nM}^{-1}$. The initial conditions for other blood factors are $P = 1400$ nM, $B = 10$ nM, $A = 3400$ nM, $G = 7000$ nM, $T = F = M = 0$ nM, $\phi_f = 10$ [10^3 mm^{-3}], and $\phi_a = 0$ [10^3 mm^{-3}]. The other initial condition initializes the velocity field.

The considered clot model was previously validated [4] against experimental data.

3. COMPUTATIONAL DOMAINS AND COMPUTATIONAL MESHES

We consider the mathematical models from Section 2 in three different types of moving domains: a right ventricle, an artery bifurcation, a simplified capillary network. Each domain is represented by its computational mesh whose topological structure remains intact during motion of the domain.

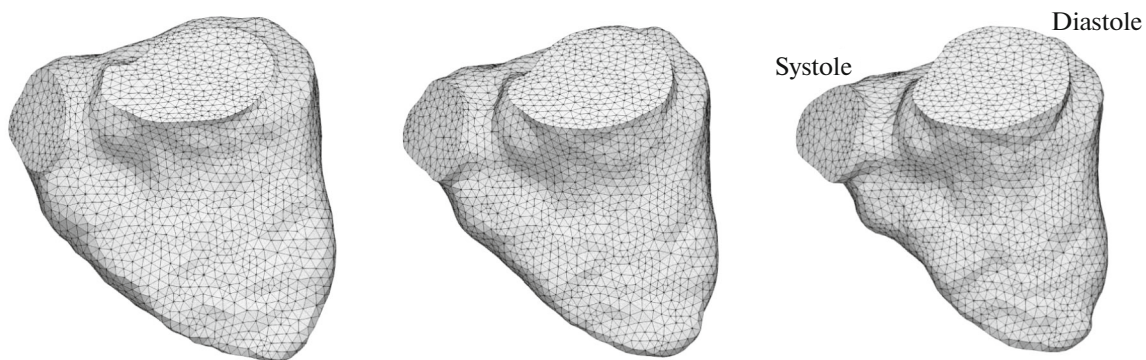
Table 1. Coefficients for the blood coagulation chemical kinetics collected in [4]

Coefficient	Source	Value	Units
k_1	[4]	1.5×10^{-4}	$10^{-3} \text{ mm}^3 \text{ s}^{-1}$
k_2	[15]	7.5×10^{-6}	$\text{nM}^{-1} \text{ s}^{-1}$
k_3	[4]	1.5×10^{-5}	$\text{nM}^{-1} \text{ s}^{-1}$
k_4	[4]	8×10^{-6}	$\text{nM}^{-2} \text{ s}^{-1}$
k_5	[4]	10^{-10}	$\text{nM}^{-3} \text{ s}^{-1}$
k_6	[41]	4.817×10^{-6}	$\text{nM}^{-1} \text{ s}^{-1}$
k_7	[4]	10^{-9}	$10^{-3} \text{ mm}^3 \text{ s}^{-1}$
k_8	[11]	5.2173×10^{-5}	$\text{nM}^{-1} \text{ s}^{-1}$
k_9	[41]	2.223×10^{-9}	$\text{nM}^{-1} \text{ s}^{-1}$
k_{10}	[35]	5×10^{-3}	s^{-1}
k_{11}	[35]	3160	nM
k_{12}	[4]	10^{-1}	s^{-1}
k_{13}	[18]	2×10^{-3}	$\text{nM}^{-1} \text{ s}^{-1}$
k_{14}	[19]	4×10^{-9}	$10^{-3} \text{ mm}^3 \text{ s}^{-1}$

The first domain type corresponds to the right ventricle of a patient given by time series of computer tomography scans. There are a total of 90 tetrahedral meshes over the heart cycle, for details we refer to [36, 37]. Three of them are demonstrated in Fig. 1. The tetrahedral meshes are made of 70 533 elements.

Boundary faces of the meshes belong to the ventricle's wall or to planes representing one of two valves (pulmonary and tricuspid). Blood velocity matches the wall velocity at the ventricle's wall. In systole and diastole, the valves are opened and closed instantly and reciprocally.

The second domain type is associated with an artery bifurcation, see Fig. 2. The mesh is constructed using GMSH software with the OpenCascade kernel. The tool "ThruSections" is used to construct a single blood vessel from a series of circles, and the entire domain is defined by the union of the artery and its branch using the "BooleanUnion" tool. The parameters of the circles in the Oxy plane for the artery

**Fig. 1.** The right ventricle mesh: (left) beginning of systole, (middle) middle of systole, (right) end of systole.

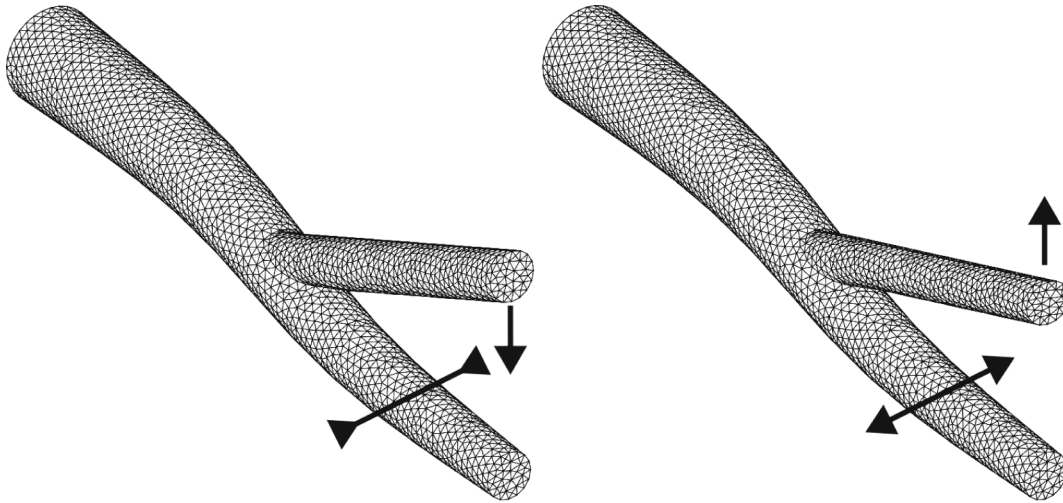


Fig. 2. The artery bifurcation: (left) beginning of cycle, (right) middle of cycle. The arrows indicate the deformation direction.

and its branch are given by central coordinates \mathbf{x}_i and radii r_i , for the artery they are

$$\mathbf{x}_k^1 = \begin{bmatrix} D \left(1 + \exp \left(\frac{5(L-kh)}{L} \right) \right)^{-1} \\ 0 \\ kh - L \end{bmatrix}, \quad r_k^1 = D \left(0.375 + 0.125 \frac{kh - L}{L} \right), \quad (7)$$

where $L = 4$ mm, $D = 1$ mm, $k = 0, \dots, 12$, and $h = L/6$; for the branch they are

$$\mathbf{x}_k^2 = \begin{bmatrix} S + \frac{L-kh}{L}(2D - S) \\ 0 \\ kh - L \end{bmatrix}, \quad r_k^2 = \frac{D}{4}, \quad (8)$$

where $S = 0.6$ mm and $k = 0, \dots, 5$.

We generated three initial quasiuniform meshes for the artery bifurcation made of 20 479, 152 326, and 1 173 233 tetrahedra.

The movement of the domain is defined analytically by translocation of the coordinates of the nodes of the initial mesh with time $\mathbf{x}_0 = [x_0, y_0, z_0]^T \rightarrow \mathbf{x}(t) = [x(t), y(t), z(t)]^T$ as follows

$$\mathbf{x}(t) = \begin{bmatrix} x_0 + 0.1 \sin(t)(x_0 - 0.15z_0 - 1.0) \\ y_0(0.9 + 0.1 \cos(t)) \\ z_0 \end{bmatrix}, \quad t \in [0; 50]. \quad (9)$$

Thus, the bifurcation pulsates 8 times within the considered time period. Figure 2 shows the domain for two different instants of the cycle.

The third domain type corresponds to a simplified capillary network, see Fig. 3. The mesh in the union of 13 vessels is constructed using GMSH software with the OpenCascade kernel in the same way as in the artery bifurcation. Each vessel of the network is described by the center \mathbf{x}_k^i and the radius r_k^i of the circles in the Oxy plane

$$\mathbf{x}_k^i = \begin{bmatrix} H \left(1 + \exp \left(\frac{xl_i - q}{dl_i} \right) \right)^{-1} + H \left(1 + \exp \left(\frac{xr_i - q}{dr_i} \right) \right)^{-1} \\ 0 \\ kh - L \end{bmatrix},$$

Table 2. Coefficients for the simplified capillary network mesh construction

i	D_i	d_i	xl_i	xr_i	dl_i	dr_i	N_i
1	0.7	0.3	17	13	4	4	18
2	0.6	0.35	-17	-13	4	4	18
3	0.25	0.1	10	5	6	5	20
4	0.25	0.2	-10	-5	4	7	20
5	0.25	0.15	10	-9	5	1	80
6	0.2	0.15	-10	10	3	5	25
7	0.15	0.1	20	-2	4	6	30
8	0.15	0.1	-17	7	4	2	50
9	0.15	0.1	-17	-5	2	6	30
10	0.15	0.1	2	12	2	8	50
11	0.15	0.1	-2	-12	8	2	35
11	0.15	0.1	0	-9	4	4	30
11	0.15	0.1	6	0	4	4	30

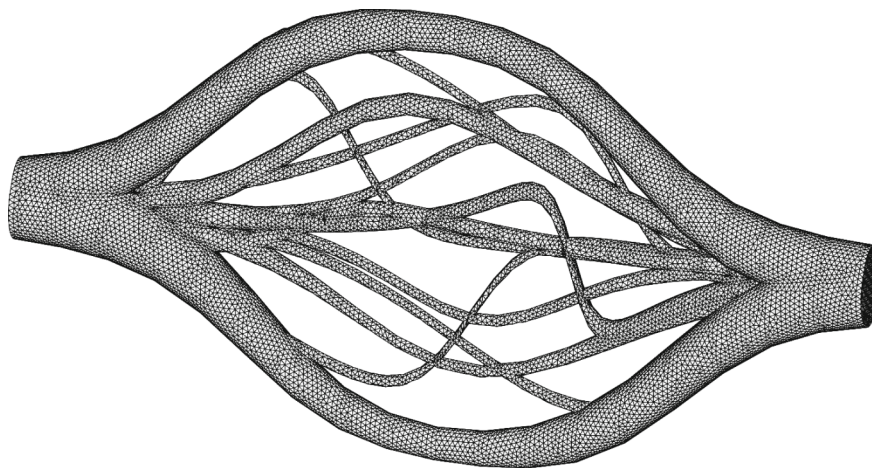
$$r_k^i = D_i + \frac{2(d_i - D_i)}{1 + \exp(0.01q^2)}, \quad q = \frac{kh - L}{L}, \quad (10)$$

where $L = 8$ mm, $H = 4$ mm, $h = 2L/N_i$, $k = 0, \dots, N_i$ is the circle index, and $i = 1, \dots, 13$ is the vessel index. The parameters for each blood vessel of the network are collected in Table 2. The quasiuniform mesh for the capillary network is made of 156 852 tetrahedra.

The translocation of the mesh nodes $\mathbf{x}(t) = [x_0, y_0(0.95 + 0.05 \cos(t)), z_0]^T$ defines the domain movement.

4. DISCRETIZATION METHOD

The four-dimensional finite-volume method is used to discretize (1), (3), and (4) with \mathbf{u} , p , and additional scalar variables $c \in \{\varphi, \mu, P, T, B, A, G, F, \phi_f, \phi_a\}$ collocated at cell centers. The detailed description of the four-dimensional discretization of the finite-volume method can be found in [9, 10, 32].

**Fig. 3.** The mesh for the simplified capillary network.

Here we just outline the approach. First, we transform (1), (3), and (4) into expressions with the four-gradient.

The Navier–Stokes system (1) is transformed into

$$\begin{pmatrix} \mathbf{u}\mathbf{u}^T - \nu_b (\nabla\mathbf{u} + \nabla\mathbf{u}^T) + p\mathbb{I} & \mathbf{u} \\ \mathbf{u}^T & 0 \end{pmatrix} \begin{pmatrix} \nabla \\ \partial_t \end{pmatrix} = \begin{pmatrix} \mathbf{0} \\ 0 \end{pmatrix}. \tag{11}$$

The boundary condition for (11) contained the right-hand side γ which is modified by $\gamma := \gamma + \boldsymbol{\alpha}\mathbf{w}$, where \mathbf{w} is the velocity of $\partial\Omega$.

The Navier–Stokes–Cahn–Hilliard system (3) can also be translated into a four-dimensional formulation as follows

$$\begin{pmatrix} \mathbf{u}\mathbf{u}^T - \nu(\varphi) (\nabla\mathbf{u} + \nabla\mathbf{u}^T) + p\mathbb{I} & \mathbf{u} \\ \mathbf{u}^T & 0 \\ \varphi\mathbf{u}^T - \epsilon M(\varphi)\nabla\mu^T & \varphi \\ -\epsilon\nabla\varphi^T & 0 \end{pmatrix} \begin{pmatrix} \nabla \\ \partial_t \end{pmatrix} = \begin{pmatrix} \mathbf{0} \\ 0 \\ 0 \\ \frac{\varphi^3 - \varphi}{\epsilon} - \mu \end{pmatrix}. \tag{12}$$

The Navier–Stokes–Brinkman system with coagulation chemical kinetics (4) is transformed into:

$$\begin{pmatrix} \mathbf{u}\mathbf{u}^T - \nu_b (\nabla\mathbf{u} + \nabla\mathbf{u}^T) + p\mathbb{I} & \mathbf{u} \\ \mathbf{u}^T & 0 \\ P\mathbf{u}^T - D\nabla P^T & P \\ T\mathbf{u}^T - D\nabla T^T & T \\ B\mathbf{u}^T - D\nabla B^T & B \\ A\mathbf{u}^T - D\nabla A^T & A \\ G\mathbf{u}^T - D\nabla G^T & G \\ F\mathbf{u}^T - D\nabla F^T & F \\ k(\phi_f, \phi_a)\phi_f\mathbf{u}^T - k(\phi_f, \phi_a)D_p\nabla\phi_f^T & \phi_f \\ k(\phi_f, \phi_a)\phi_a\mathbf{u}^T - k(\phi_f, \phi_a)D_p\nabla\phi_a^T & \phi_a \\ \mathbf{0}^T & M \end{pmatrix} \begin{pmatrix} \nabla \\ \partial_t \end{pmatrix} = \begin{pmatrix} -\frac{\nu_b}{K}\mathbf{u} \\ 0 \\ \mathbf{R}_c \end{pmatrix}, \tag{13}$$

where \mathbf{R} is the chemical kinetics system representing coagulation reactions

$$\mathbf{R}_c = \begin{pmatrix} -(k_1\phi_a + k_2B + k_3T + k_4T^2 + k_5T^3)P \\ (k_1\phi_a + k_2B + k_3T + k_4T^2 + k_5T^3)P - k_6AT \\ (k_7\phi_a + k_8T)(B^0 - B) - k_9AB \\ -k_6AT - k_9AB \\ -k_{10}TG(k_{11} + G)^{-1} \\ k_{10}TG(k_{11} + G)^{-1} - k_{12}F \\ -(k_{13}T + k_{14}\phi_a)\phi_f \\ (k_{13}T + k_{14}\phi_a)\phi_a \\ k_{12}F \end{pmatrix}. \tag{14}$$

Systems (11), (12), and (13) can be written in a common general form

$$\mathbf{F} \begin{pmatrix} \nabla \\ \partial_t \end{pmatrix} = \mathbf{R}, \quad (15)$$

where \mathbf{F} is the matrix of size $m \times 4$ and R is the right-hand side of size $m \times 1$, $m = \{4, 6, 13\}$ for (11), (12), and (13), respectively.

Second, assuming that the topological structure of the computational mesh remains intact during the movement and therefore there is a single time layer in the fourth dimension for all mesh cells ω , we define a four-dimensional prism $\omega(t) = \omega_n \cup \omega_{n+1}$ connecting two representative volumes ω_n and ω_{n+1} at time steps t_n and t_{n+1} , respectively. The four-dimensional surface of $\omega(t)$ is denoted by $\partial\omega(t)$. Integrating (15) over $\omega(t)$ and applying the Ostrogradsky–Gauss theorem [16, 42], we transform the volumetric integral of (15) into a space-time surface integral

$$\int_{\omega(t)} \mathbf{F} \begin{pmatrix} \nabla \\ \partial_t \end{pmatrix} dV(t) = \oint_{\partial\omega(t)} \mathbf{F} d\mathbf{S}(t) = \int_{\omega(t)} \mathbf{R} dV(t). \quad (16)$$

The approximation with the second-order accuracy of the surface integral in (16) with a single integration point at the middle of four-dimensional faces is

$$\oint_{\partial\omega(t)} \mathbf{F} d\mathbf{S}(t) \approx \sum_{\sigma(t) \in \partial\omega(t)} |\sigma(t)| \mathbf{F}|_{\mathbf{x}_{\sigma(t)}} \begin{pmatrix} \mathbf{n} \\ n_t \end{pmatrix}, \quad (17)$$

where $\sigma(t) = \sigma_n \cup \sigma_{n+1}$ is the four-dimensional face made of faces σ_n and σ_{n+1} at time moments t_n and t_{n+1} . Its geometric center in four dimensions is given by $\mathbf{x}_{\sigma(t)} = \left[\frac{\mathbf{x}_{\sigma_n} + \mathbf{x}_{\sigma_{n+1}}}{2}, \frac{t_n + t_{n+1}}{2} \right]^T$, its area is defined by $|\sigma(t)| = (t_{n+1} - t_n) \frac{|\sigma_{n+1}| + |\sigma_n|}{2}$, its three-dimensional outer normal $\mathbf{n} = \frac{\mathbf{n}_{\sigma_{n+1}} + \mathbf{n}_{\sigma_n}}{2}$ is the average of outer normals to σ_n and σ_{n+1} and the fourth dimension of the normal is given by $n_t = -\frac{\mathbf{n} \cdot (\mathbf{x}_{\sigma_{n+1}} - \mathbf{x}_{\sigma_n})}{t_{n+1} - t_n} = -\mathbf{n} \cdot \mathbf{w}_{\sigma(t)}$, where $\mathbf{w}_{\sigma(t)}$ is the approximation to the mesh movement velocity at the face center.

The degrees of freedom are located at the centers of 3D cells (representative elementary volumes) ω_n at time level t_n . There are two four-dimensional faces in $\partial\omega(t)$ that entirely lay at the temporal boundaries t_n and t_{n+1} . These faces correspond to $\sigma(t) \in \partial\omega(t) \cap t_n = \omega_n$ and $\sigma(t) \in \partial\omega(t) \cap t_{n+1} = \omega_{n+1}$ with the normals $[\mathbf{0}^T, -1]^T$ and $[\mathbf{0}^T, 1]^T$ and areas $|\omega_n|$ and $|\omega_{n+1}|$, respectively. For the computation of the fluxes at these faces, the degrees of freedom are taken from representative volumes at corresponding time levels. If one uses the approximation $\mathbf{F}|_{\mathbf{x}_{\sigma(t)}}$ by averaging degrees of freedom from time levels t_n and t_{n+1} , he arrives at the four-dimensional counterpart of the second-order Crank–Nicolson method. In this work, for the sake of stability, we use the approximation $\mathbf{F}|_{\mathbf{x}_{\sigma_{n+1}}}$ from time level t_{n+1} , resulting in the four-dimensional counterpart of the first-order backward Euler method.

Third, let C represent the vector of m degrees of freedom collocated at the center of ω_{n+1} , and $C \otimes \begin{bmatrix} \nabla \\ \partial_t \end{bmatrix}$ represent its $4m$ gradient vector. We note that for problem (11) the degrees of freedom are $C = [u, v, w, p]^T$, for problem (12) they are $C = [u, v, w, p, \varphi, \mu]^T$, and for problem (13) they are $C = [u, v, w, p, P, T, B, A, G, F, \phi_f, \phi_a, M]^T$. Let us decompose the flux \mathbf{F} into a hyperbolic part and an elliptic part: $\mathbf{F} = \mathbf{F}_H + \mathbf{F}_E$. The elliptic part of the flux takes the form

$$\mathbf{F}_E \begin{bmatrix} \mathbf{n} \\ n_t \end{bmatrix} = -\mathbb{I} \otimes \begin{bmatrix} \mathbf{n} \\ n_t \end{bmatrix}^T \mathbb{E} \left(C \otimes \begin{bmatrix} c\nabla \\ \partial_t \end{bmatrix} \right), \quad (18)$$

where \mathbb{E} is an $m \times 4m$ matrix. For the Navier–Stokes equations (11) matrix \mathbb{E} is given by

$$\mathbb{E} = \begin{bmatrix} \nu_b \mathbb{I} \\ 0 \end{bmatrix} \otimes [\mathbf{n}^T \ 0] + [\mathbf{n}^T \ 0] \otimes \begin{bmatrix} \nu_b \mathbb{I} \\ 0 \end{bmatrix}, \tag{19}$$

and for the Navier–Stokes–Cahn–Hilliard equations (12) it is given by

$$\mathbb{E} = \begin{bmatrix} \nu(\varphi) \mathbb{I} \\ 0 \\ \epsilon M(\varphi) \\ \epsilon \end{bmatrix} \otimes [\mathbf{n}^T \ 0] + [\mathbf{n}^T \ 0] \otimes \begin{bmatrix} \nu(\varphi) \mathbb{I} \\ 0 \\ 0 \\ 0 \end{bmatrix}. \tag{20}$$

The expression for matrix \mathbb{E} in the case of the Navier–Stokes–Brinkman equations coupled with coagulation equations (13) is given in [32], and we omit it for the sake of brevity.

We assume that matrix \mathbb{E} can be approximated by a constant matrix at each cell of the mesh, and the degrees of freedom are linear continuous functions over each face σ of the mesh, whereby their gradient is constant. Let degrees of freedom C_1 be collocated in four-dimensional barycenter \mathbf{x}_1 of a representative volume ω_1 at time level t_{n+1} , and unknowns C_σ be collocated in four-dimensional barycenter \mathbf{x}_σ of the face $\sigma \in \partial\omega_1$ at time level t_{n+1} with four-dimensional outer normal $[\mathbf{n}^T, n_t]^T$. We can decompose the gradient in ω_1 in a proximity of the face σ by the sum of its normal and transversal components

$$C_1 \otimes \begin{bmatrix} \nabla \\ \partial_t \end{bmatrix} = \frac{C_\sigma - C_1}{r_1} \otimes \begin{bmatrix} \mathbf{c}\mathbf{n} \\ n_t \end{bmatrix} + \left(\mathbb{I} \otimes \mathbb{I} - \frac{1}{r_1} \mathbb{I} \otimes \begin{bmatrix} \mathbf{n} \\ n_t \end{bmatrix} (\mathbf{x}_\sigma - \mathbf{x}_1)^T \right) C_1 \otimes \begin{bmatrix} \nabla \\ \partial_t \end{bmatrix}, \tag{21}$$

where $r_1 = [\mathbf{n}^T, n_t] (\mathbf{x}_\sigma - \mathbf{x}_1)$ is the distance from the cell center \mathbf{x}_1 to the face σ . Substituting (21) in (18) results in the following approximation of the elliptic part of the flux

$$\mathbf{F}_E|_{\mathbf{x}_\sigma} \begin{bmatrix} \mathbf{n} \\ n_t \end{bmatrix} \approx \Lambda_1 (C_1 - C_f) - \Gamma_1^T \left(C_1 \otimes \begin{bmatrix} \nabla \\ \partial_t \end{bmatrix} \right), \tag{22}$$

where Λ_1 is $m \times m$ matrix and Γ_1 is $m \times 4m$ matrix

$$\Lambda_1 = \frac{1}{r_1} \mathbb{I} \otimes \begin{bmatrix} \mathbf{c}\mathbf{n} \\ n_t \end{bmatrix}^T \mathbb{E}_1 \mathbb{I} \otimes \begin{bmatrix} \mathbf{n} \\ n_t \end{bmatrix},$$

$$\Gamma_1^T = \mathbb{I} \otimes \begin{bmatrix} \mathbf{n} \\ n_t \end{bmatrix}^T \mathbb{E}_1 - \Lambda_1 \otimes (\mathbf{x}_\sigma - \mathbf{x}_1)^T. \tag{23}$$

Note that matrix Γ_1^T requires only transversal part of the gradient.

For the hyperbolic part of flux \mathbf{F}_H , we use the second-order Taylor series around \mathbf{x}_1 for the inertia term:

$$\mathbf{u}\mathbf{u}^T \mathbf{n}|_{\mathbf{x}_\sigma} \approx \mathbf{u}\mathbf{u}^T \mathbf{n}|_{\mathbf{x}_1} + \frac{\partial \mathbf{u}\mathbf{u}^T \mathbf{n}}{\partial \mathbf{u}^T} \Big|_{\mathbf{x}_1} \otimes (\mathbf{x}_\sigma - \mathbf{x}_1)^T \left(\mathbf{u} \otimes \begin{bmatrix} \nabla \\ \partial_t \end{bmatrix} \right) \Big|_{\mathbf{x}_1}$$

$$= \frac{1}{2} (\mathbf{u}_1^T \mathbf{n} \mathbb{I} + \mathbf{u}_1 \mathbf{n}^T) (2\mathbf{u}_\sigma - \mathbf{u}_1) = Q_1 (2\mathbf{u}_\sigma - \mathbf{u}_1), \tag{24}$$

where Q_1 is approximated at time level t_n via Oseen linearization, *i.e.* using \mathbf{u}_1 from the time level t_n . For the Navier–Stokes system (11) with the account of (24), the approximation of the hyperbolic part of the flux takes the form

$$\mathbf{F}_H|_{\mathbf{x}_\sigma} \approx \begin{bmatrix} 2Q_1 + \mathbb{I}n_t & \mathbf{n} \\ \mathbf{n}^T & \end{bmatrix} \begin{bmatrix} \mathbf{u}_\sigma \\ p_\sigma \end{bmatrix} - \begin{bmatrix} Q_1 & \mathbf{0} \\ \mathbf{0}^T & \end{bmatrix} \begin{bmatrix} \mathbf{u}_1 \\ p_1 \end{bmatrix}, \tag{25}$$

whereas for the Navier–Stokes–Cahn–Hilliard system (12) it becomes

$$\mathbf{F}_H|_{\mathbf{x}_\sigma} \approx \begin{bmatrix} 2Q_1 + \mathbb{I}n_t & \mathbf{n} & \mathbf{0} & \mathbf{0} \\ \mathbf{n}^T & & & \\ \mathbf{0}^T & \mathbf{n}^T \mathbf{u}_\sigma + n_t & & \\ \mathbf{0}^T & & & \end{bmatrix} \begin{bmatrix} \mathbf{u}_\sigma \\ p_\sigma \\ \varphi_\sigma \\ \mu_\sigma \end{bmatrix} - \begin{bmatrix} Q_1 & \mathbf{0} & \mathbf{0} & \mathbf{0} \\ \mathbf{0}^T & & & \\ \mathbf{0}^T & & & \\ \mathbf{0}^T & & & \end{bmatrix} \begin{bmatrix} \mathbf{u}_1 \\ p_1 \\ \varphi_1 \\ \mu_1 \end{bmatrix}. \tag{26}$$

For brevity, we omit the expressions for the Navier–Stokes–Brinkman system with chemical kinetics (13) and refer the interested reader to [32]. In general, the hyperbolic part of flux is written in the form

$$\mathbf{F}_H|_{\mathbf{x}_\sigma} \approx \Psi_1^\sigma C_\sigma - \Psi_1^\omega C_1 \tag{27}$$

with appropriate matrices $\Psi_1^\sigma, \Psi_1^\omega$. Note that in (25) and (26) Ψ_1^σ depends on unknown \mathbf{u}_σ , a component of unknown C_σ . At the boundary mesh face, one can derive C_σ from the system of boundary conditions. For interior mesh face, although it is possible to decouple the dependence using second-order Taylor series, by analogy with (24), here we use the fact that C_σ can be obtained independently, see below. Combination of (22) and (27) gives

$$\mathbf{F}|_{\mathbf{x}_\sigma} \approx (\Lambda_1 - \Psi_1^\omega)C_1 - (\Lambda_1 - \Psi_1^\sigma)C_\sigma - \Gamma_1^T \left(C_1 \otimes \begin{bmatrix} \nabla \\ \partial_t \end{bmatrix} \right). \tag{28}$$

In (28), the instability of the method manifests itself when matrices $\Lambda_1 - \Psi_1^\omega$ or $\Lambda_1 - \Psi_1^\sigma$ have negative eigenvalues. In order to dump both the convective instability and the saddle-point instability, we subtract from (28) the following expression

$$\mathbf{0} = \Sigma_1 (C_\sigma - C_1) - \Sigma_1 \otimes (\mathbf{x}_\sigma - \mathbf{x}_1)^T C_1 \otimes \begin{bmatrix} \nabla \\ \partial_t \end{bmatrix}, \tag{29}$$

where Σ_1 is an $m \times m$ stabilization matrix. Analytical expressions of such matrices are derived from the eigenvalue decomposition and can be found in [27, 28, 30–33].

Combination of (28) with (29) gives

$$\mathbf{F}|_{\mathbf{x}_\sigma} \approx \Lambda_1^\omega C_1 - \Lambda_1^\sigma C_\sigma - \left(\Gamma_1^T - \Sigma_1 \otimes (\mathbf{x}_\sigma - \mathbf{x}_1)^T \right) C_1 \otimes \begin{bmatrix} \nabla \\ \partial_t \end{bmatrix}, \tag{30}$$

where $\Lambda_1^\omega = \Lambda_1 + \Sigma_1 - \Psi_1^\omega, \Lambda_1^\sigma = \Lambda_1 + \Sigma_1 - \Psi_1^\sigma$. For the internal face $\sigma = \omega_1 \cap \omega_2$, we repeat the above steps and construct another approximation for the flux at σ in cell ω_2 :

$$\mathbf{F}|_{\mathbf{x}_\sigma} \approx \Lambda_2^\sigma C_\sigma - \Lambda_2^\omega C_2 - \left(\Gamma_2^T - \Sigma_2 \otimes (\mathbf{x}_2 - \mathbf{x}_\sigma)^T \right) C_2 \otimes \begin{bmatrix} \nabla \\ \partial_t \end{bmatrix}. \tag{31}$$

Continuity of fluxes (30) and (31) at σ yields an expression for the unknown C_σ :

$$C_\sigma = (\Lambda_1^\sigma + \Lambda_2^\sigma)^{-1} (\Lambda_1^\omega C_1 + \Lambda_2^\omega C_2) - (\Lambda_1^\sigma + \Lambda_2^\sigma)^{-1} \left(\Gamma_1^T - \Sigma_1 \otimes (\mathbf{x}_\sigma - \mathbf{x}_1)^T \right) C_1 \otimes \begin{bmatrix} \nabla \\ \partial_t \end{bmatrix}$$

$$+ (\Lambda_1^\sigma + \Lambda_2^\sigma)^{-1} \left(\Gamma_2^T - \Sigma_2 \otimes (\mathbf{x}_2 - \mathbf{x}_\sigma)^T \right) C_2 \otimes \begin{bmatrix} \nabla \\ \partial_t \end{bmatrix}. \tag{32}$$

Following this approach, we derive \mathbf{u}_σ from the continuity of the Navier–Stokes part of the flux. Vector \mathbf{u}_σ is used to define the advective velocity $\mathbf{n}^T \mathbf{u}_\sigma$ in Ψ_1^σ for the Navier–Stokes–Cahn–Hilliard system (26) and in Navier–Stokes–Brinkman system with chemical kinetics. Finally, we substitute C_σ into either (30) or (31) to obtain the flux.

For the internal face $\sigma = \omega_1 \cap \omega_2$, the flux reads as

$$\begin{aligned} \mathbf{F}|_{\mathbf{x}_\sigma} &\approx \Lambda_1^\sigma (\Lambda_1^\sigma + \Lambda_2^\sigma)^{-1} \Lambda_2^\sigma (C_1 - C_2) \\ &- \Lambda_1^\sigma (\Lambda_1^\sigma + \Lambda_2^\sigma)^{-1} \left(\Gamma_1^T - \Sigma_1 \otimes (\mathbf{x}_\sigma - \mathbf{x}_1)^T \right) C_1 \otimes \begin{bmatrix} \nabla \\ \partial_t \end{bmatrix} \\ &- \Lambda_2^\sigma (\Lambda_1^\sigma + \Lambda_2^\sigma)^{-1} \left(\Gamma_2^T - \Sigma_2 \otimes (\mathbf{x}_2 - \mathbf{x}_\sigma)^T \right) C_2 \otimes \begin{bmatrix} \nabla \\ \partial_t \end{bmatrix}. \end{aligned} \tag{33}$$

The gradient $C_1 \otimes \begin{bmatrix} \nabla \\ \partial_t \end{bmatrix}$ at cell ω_1 is calculated using the least-squares method with all degrees of freedom from cells sharing at least a node with ω_1 and from adjacent boundary faces $\sigma \in \partial\omega_1 \cap \partial\Omega$.

The right-hand side in (16) is approximated with the simplest quadrature

$$\int_{\omega(t)} \mathbf{R} dV(t) \approx |\omega(t)| \mathbf{R}|_{\mathbf{x}_{\omega(t)}}, \tag{34}$$

where the four-dimensional volume is given by $|\omega(t)| = (t_{n+1} - t_n) \frac{|\omega_{n+1}| + |\omega_n|}{2}$ and the cell center is $\mathbf{x}_{\omega(t)} = \left[\frac{\mathbf{x}_{\omega_{n+1}} + \mathbf{x}_{\omega_n}}{2}, \frac{t_{n+1} + t_n}{2} \right]$.

For stability purposes, the double-well potential term of the Navier–Stokes–Cahn–Hilliard equations (12) is discretized using the convex approximation [20]:

$$\frac{\varphi^3 - \varphi}{\epsilon} \Big|_{\mathbf{x}_{\omega(t)}} \approx \frac{(\varphi^{n+1})^3 - \varphi^n}{\epsilon}, \tag{35}$$

whereas the coagulation reaction system is discretized using a matrix-weighted combination of backward and forward Euler methods [7]:

$$\mathbf{R}_c|_{\mathbf{x}_{\omega(t)}} \approx W \mathbf{R}_c(t_{n+1}) + (\mathbb{I} - W) \mathbf{R}_c(t_n), \tag{36}$$

where matrix $W = \theta(J)$ is obtained through spectral decomposition of the Jacobian $J = \partial \mathbf{R}_c / \partial C^T$. Using $\theta(z) = \frac{1}{z} - \frac{1}{\exp(z) - 1}$, the method reproduces the first-order exponential integrator. Further details can be found in [7, 32]. The Darcy term $\frac{\nu_b}{K} \mathbf{u}$ is approximated at the next time level t_{n+1} .

To summarize, the temporal discretization is equivalent to the first-order backward Euler scheme in time, where the Oseen linearization is used for the advective term, the spatial discretizations with cell-centered collocation of unknowns result in block-structured linear systems with block sizes 4, 6, and 13 for equations (1), (3), and (4), respectively.

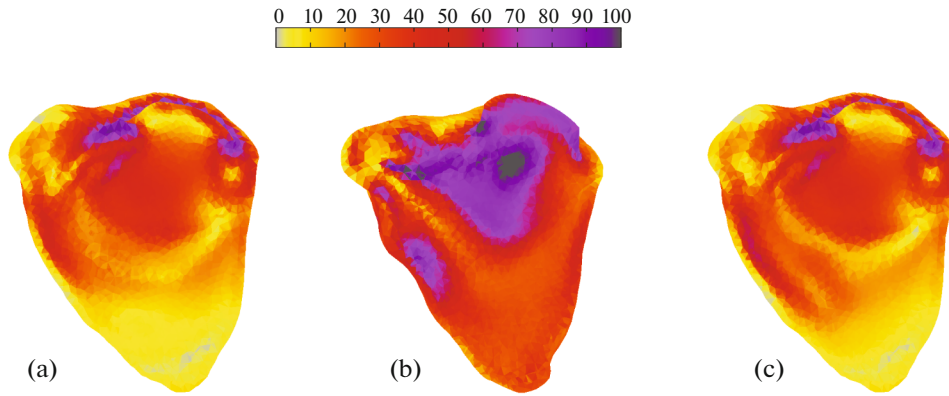


Fig. 4. Velocity magnitude mm s^{-1} at the (a) beginning of systole, (b) beginning of diastole, (c) end of diastole.

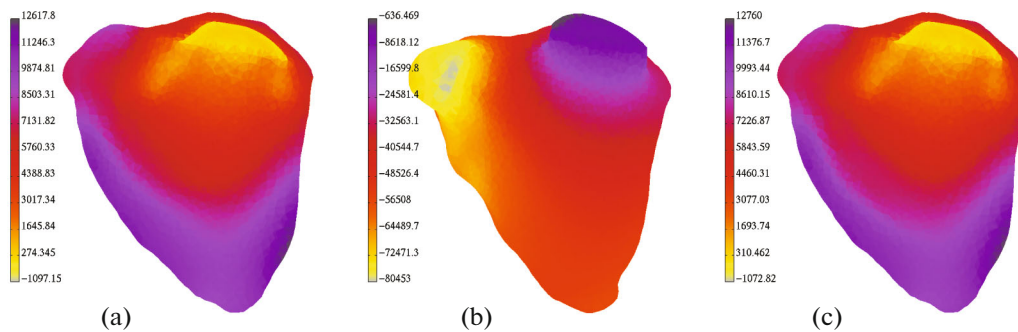


Fig. 5. Pressure at the (a) beginning of systole, (b) beginning of diastole, (c) end of diastole.

5. SIMULATIONS

5.1. Simulations in the Right Ventricle

The first problem is concerned with the blood flow in the moving right ventricle governed by equations (1) over the time period $t \in [0, 4.5]$ s with time step $\Delta t = 0.01$ s. The interval between moving mesh frames $\delta t = 0.01$ s coincides with the time step, a single cycle takes 0.9 s and the simulation is performed for 5 cycles. At the initial state the velocity and pressure are zero. The velocity magnitude evolution and the pressure evolution over the last cycle are demonstrated in the colored slice of the mesh in Figs. 4 and 5, respectively. The evolution of minimal and maximal pressure and velocity magnitude over all five cycles is given in Fig. 6. The boundary conditions in this problem are similar to those in [32]: on the walls and closed valve of the ventricle the no-slip condition $\alpha_{\perp} = \alpha_{\parallel} = 1$, $\beta_{\perp} = \beta_{\parallel} = 0$, $\gamma = \mathbf{0}$ is imposed, whereas on the open valve the directional do-nothing condition $\alpha_{\perp} = \alpha_{\parallel} = \frac{1}{2} (|\mathbf{n}^T \mathbf{u} + n_t| - (\mathbf{n}^T \mathbf{u} + n_t))$, $\beta_{\perp} = \beta_{\parallel} = 1$, $\gamma = \mathbf{0}$ is imposed. The initial mesh belongs to the box $[14, 45.7] \times [-248.5, -217.6] \times [1314.3, 1348]$.

The linear systems generated for this problem are named in the followup paper [17] by **Hout**.

Problem (3) in the ventricle domain corresponds to the scenario of the clot-in-transit [23]. We set the initial conditions by $\varphi = \text{sgn} \left(10 - \sqrt{(x - 30)^2 + (y - 235)^2 + (z - 1330)^2} \right)$ and zero chemical potential μ . The simulation is performed over 3 cardiac cycles, $t \in [0, 2.7]$, with time step $\Delta t = 0.005$. The movement of the clot over one cycle is demonstrated in Figs. 7 and 8. The clot is slowly washed out the domain until the entire clot disappears through the pulmonary valve. Impact of the clot presence is shown in Fig. 9: due to the clot pressure spikes become stronger.

The linear systems generated for this problem are named in the followup paper [17] by **Hoch**.

The third scenario corresponds to the clot formation in the ventricle due to tissue inflammation following acute myocardial infarction [26]. For the problem (4) posed in the ventricle, we set the

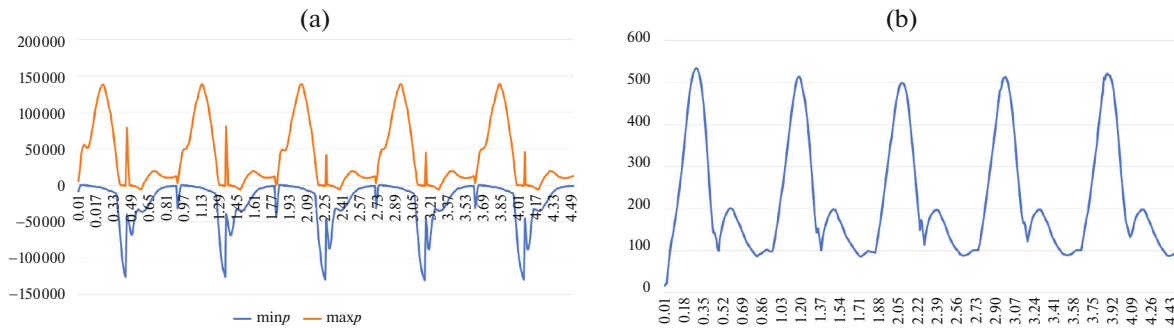


Fig. 6. Evolution of minimal and maximal pressure (a) and velocity magnitude (b).

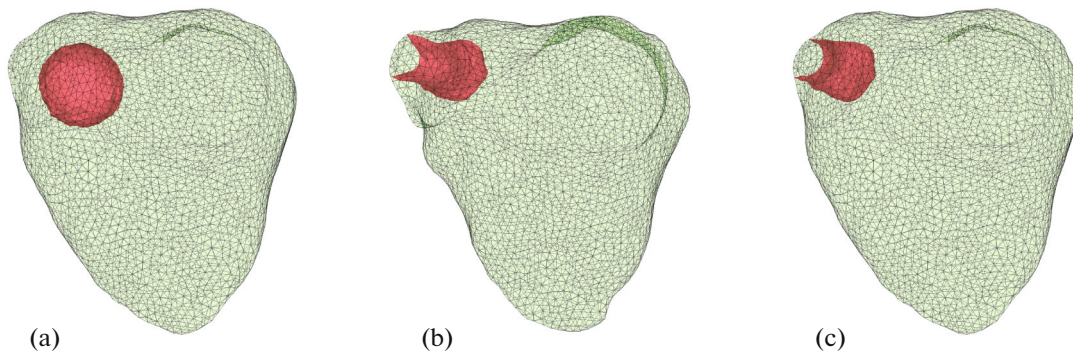


Fig. 7. Front view of clot surface $\varphi = 0$ at: (a) beginning of systole, (b) beginning of diastole, (c) end of diastole.

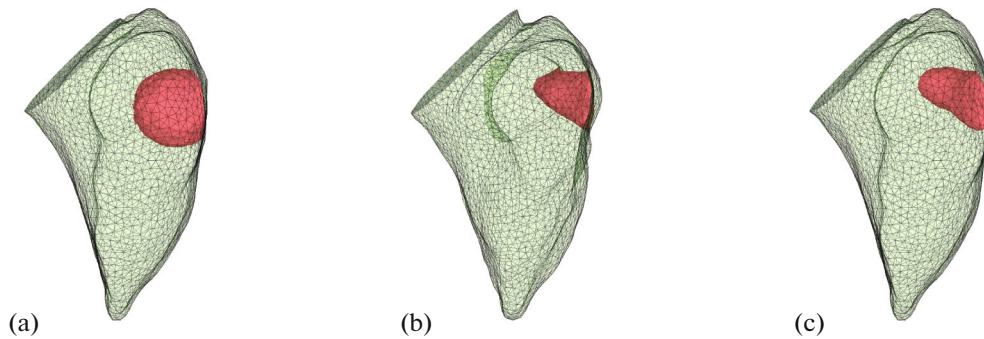


Fig. 8. Side view of clot surface $\varphi = 0$ at: (a) beginning of systole, (b) beginning of diastole, (c) end of diastole.

boundary condition at the damaged endothelium according to the model description in Section 2.2.3, where the damaged endothelium is defined (for the mesh close to the systole) at 13 boundary mesh faces satisfying $10 - \sqrt{(x - 30)^2 + (y - 235)^2 + (z - 1330)^2} > 0$, see Fig. 10a. The simulation is performed over 45 cardiac cycles, $t \in [0, 40.5]$, with the time step $\Delta t = 0.005$. The clot grows very slowly, see Fig. 10b, with the clotting factors being constantly washed out. The clotting factors ϕ_a that appear in the calculation of the permeability (5) are demonstrated in Fig. 11. The isosurface corresponding to a significant amount of tissue factor B and to the clotted zone at the final time of the simulation are shown in Fig. 12. The clot tends to occupy the ventricle more severely every cardiac cycle, but it is washed out at a high rate.

The linear systems generated for this problem are named in the followup paper [17] by **Hinj**.

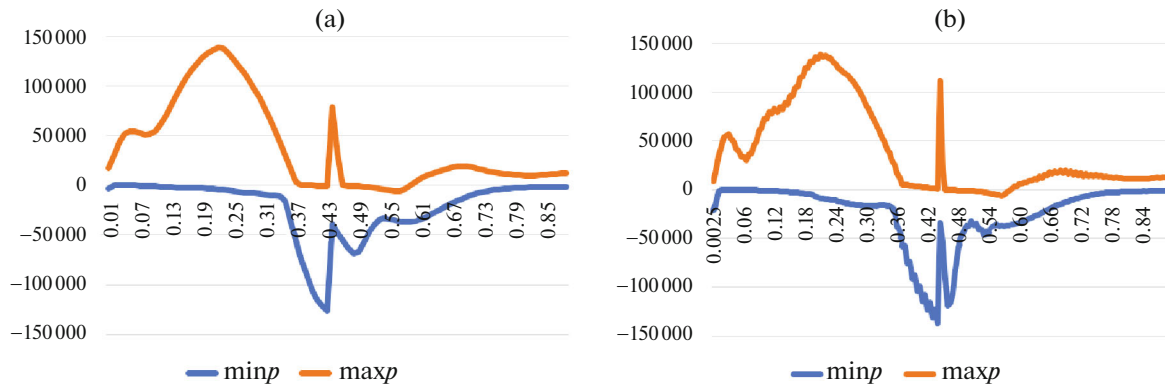


Fig. 9. Evolution of minimal and maximal pressure for a single cycle without clot (a) and with clot (b).

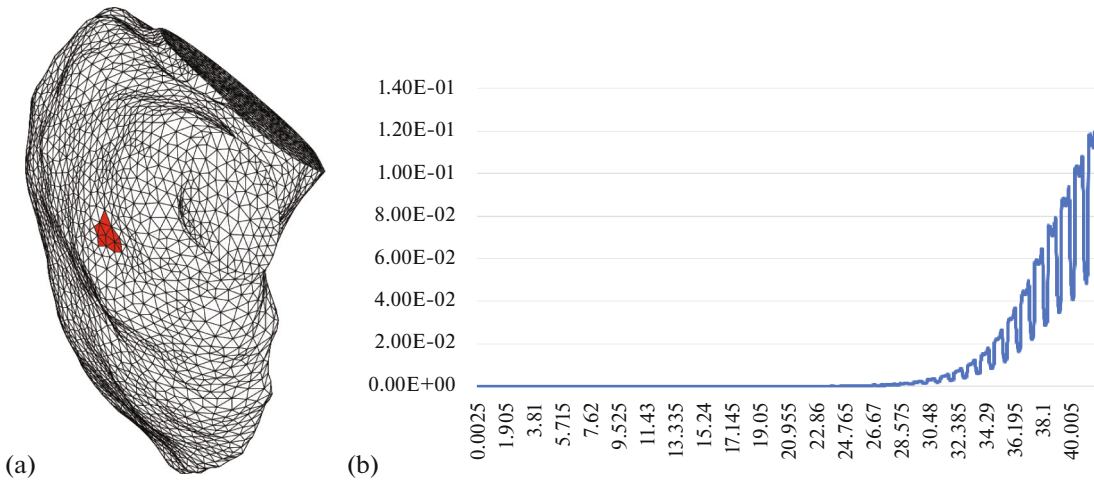


Fig. 10. Boundary corresponding to the damaged endothelium colored in red (a). Part of the ventricle volume occupied by the clot, $\times 100\%$ (b).

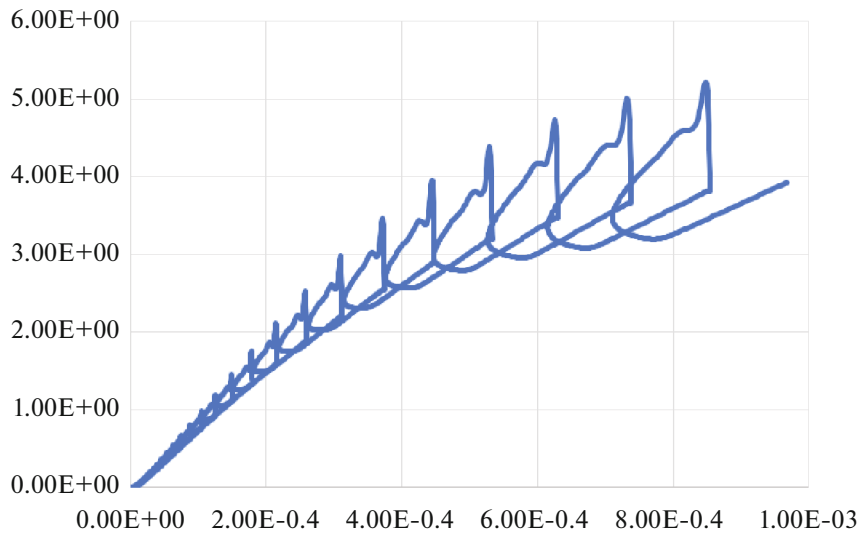


Fig. 11. Mean concentration of activated platelets ϕ_a [10^3 mm^{-3}] (left axis) against mean concentration of fibrin polymer M [nM] (bottom axis).

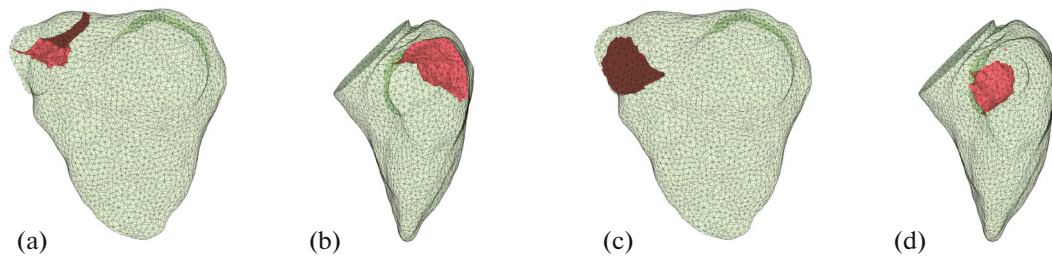


Fig. 12. Isosurface corresponding to tissue factors $B = 0.1 \text{ nM}$ (a, b) and permeability coefficient $\nu_b/K = 0.4 \text{ s}^{-1}$ (c, d). Pink and brown colors correspond to inner and outer (with respect to the clot) sides of the isosurface. Part of clot boundary touching ventricle boundary is not shown.

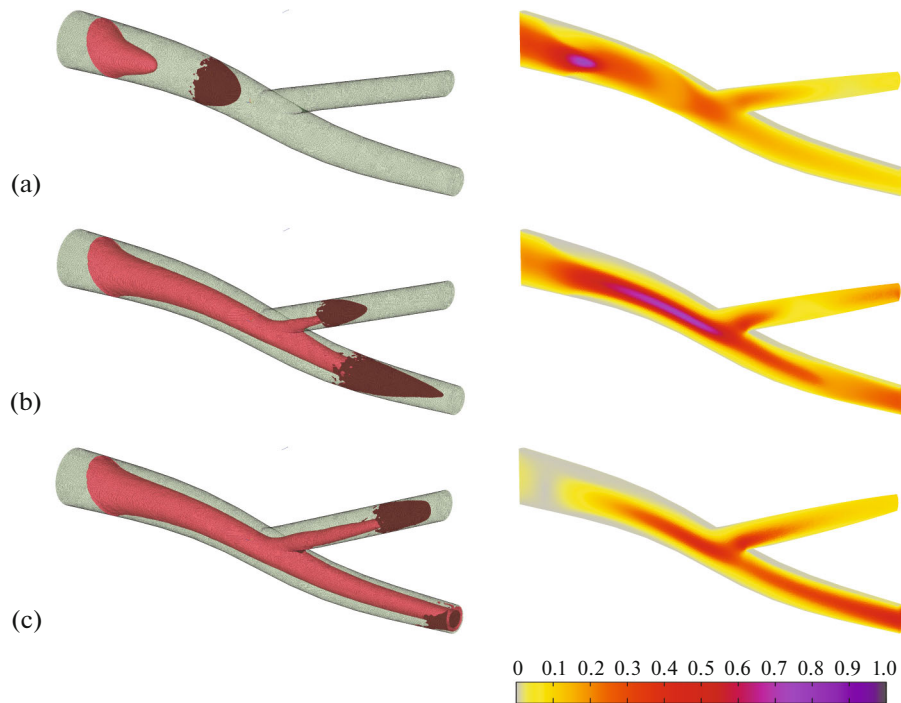


Fig. 13. Clot isosurface $\varphi = 0$ (left) and velocity magnitude $[\text{mm s}^{-1}]$ (right) at the (a) beginning of time period $t = 0 \text{ s}$, (b) middle of time period $t = 25 \text{ s}$, (c) end of time period $t = 50 \text{ s}$. Pink and brown colors correspond to inner and outer (with respect to the clot) sides of the isosurface. Part of clot boundary touching vessel boundary is not shown.

5.2. Simulations in the Artery Bifurcation

We solve numerically the Navier–Stokes–Cahn–Hilliard equations (3) in the artery bifurcation for the time period $t \in [0, 50] \text{ s}$ with time steps $\Delta t = \{0.125, 0.0625, 0.03125\}$ for the coarse, finer, and finest tetrahedral meshes with $\{20\,479, 152\,326, 1\,173\,233\}$ elements, respectively. The inflow pressure $p = 2000 \text{ mm}^2 \text{ s}^{-2}$ is set at the boundary part $\partial\Omega|_{z=-4}$, and zero outflow pressure is set at the boundary part $\partial\Omega|_{z=4}$, no-slip condition is set at the remaining part of the boundary. The clot is set by the initial value of $\varphi = \text{sgn}\left(0.5 - \sqrt{(x - 1.35)^2 + y^2 + (z - 2.5)^2}\right)$. The evolution of the clot surface and the maximal velocity on the finest mesh is displayed in Fig. 13. Initially the clot occludes the vessel. Over time it is washed out but narrows the blood vessel lumen. The maximal velocity and kinetic energy evolution throughout the simulation on the coarse, finer and finest meshes of the domain is demonstrated in Fig. 14. Although the finest mesh resolution provides higher kinetic energy, the oscillatory dynamics due to vessel wall pulsations is captured even on the coarse mesh.

The linear systems generated for this problem are named in the followup paper [17] by **Bmc1**, **Bmc2**, and **Bmc3** for the coarse, finer, and finest meshes, respectively.

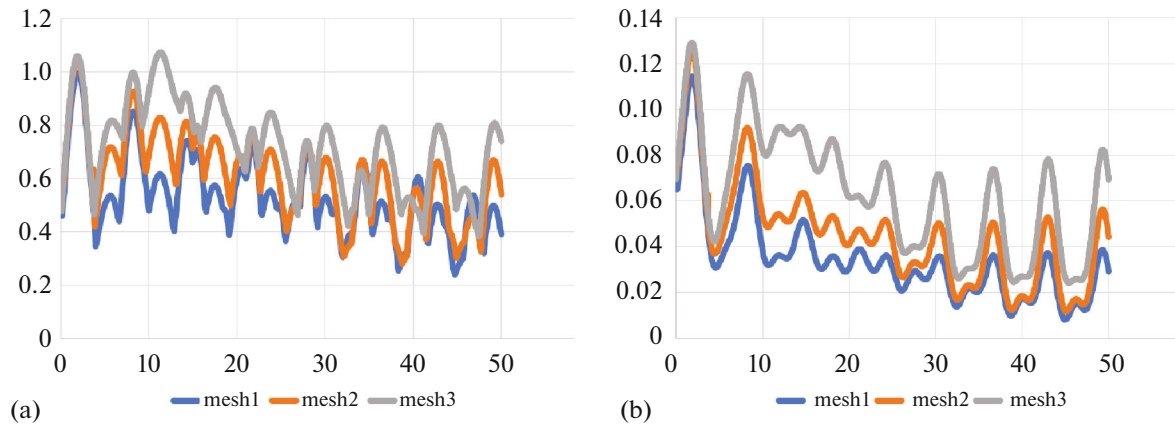


Fig. 14. Maximal velocity $[\text{mm s}^{-1}]$ (a) and density normalized kinetic energy $\frac{1}{2} \int_{\Omega} |\mathbf{u}|^2 dx$ $[\text{mm}^5 \text{s}^{-2}]$ (b) evolution for the three meshes.

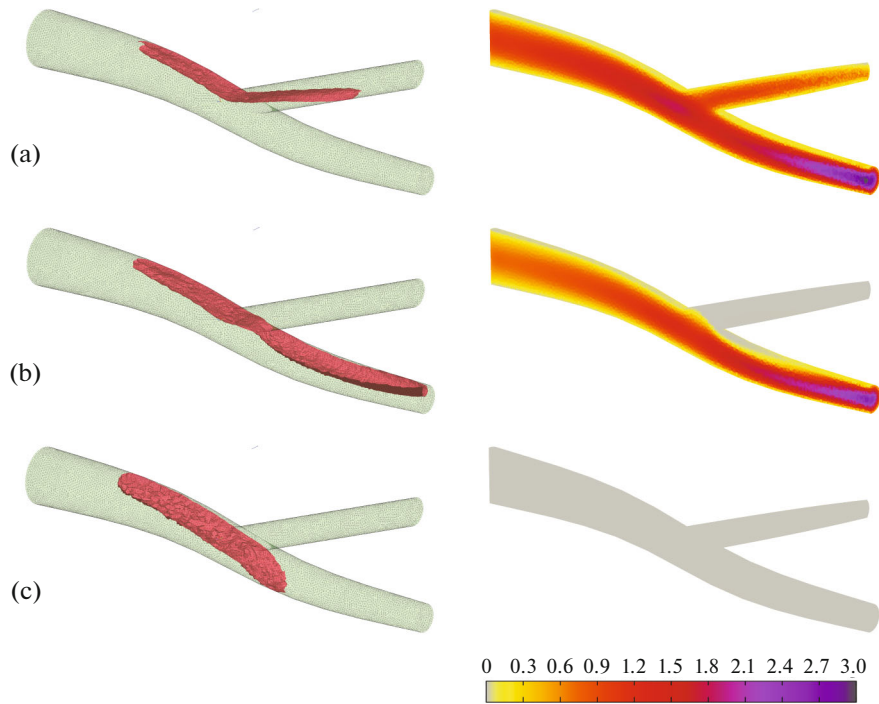


Fig. 15. Permeability isosurface $\nu_b/K = 40 \text{ s}^{-1}$ (left) and velocity magnitude $[\text{mm s}^{-1}]$ (right) (a) before complete occlusion $t = 35 \text{ s}$, (b) right before complete occlusion $t = 50 \text{ s}$, (c) after complete occlusion $t = 65 \text{ s}$. Pink and brown colors correspond to inner and outer (with respect to the clot) sides of the isosurface. Part of clot boundary touching vessel boundary is not shown.

For the Navier–Stokes–Brinkman problem with coagulation chemical kinetics (4) in the artery bifurcation, we consider the time period $t \in [0, 150] \text{ s}$ with the same time steps $\Delta t = \{0.125, 0.0625, 0.03125\}$ for the same coarse and finer tetrahedral meshes. The domain does not move in this case. The case with the finest mesh ended earlier at $t = 94 \text{ s}$ due to time limit. The damaged endothelium is defined at the part of the boundary $\partial\Omega$ satisfying $\sqrt{(x - 1.35)^2 + y^2 + (z - 2)^2} < 0.5$. The evolution of the clot surface and the maximal velocity on the finer mesh is displayed in Fig. 15. Over time the clot occludes the entire blood vessel. The maximal velocity, kinetic energy, and volumetric occlusion evolution throughout the simulation on the coarse and finer meshes are demonstrated in Fig. 16. The results suggest that the solution on the coarse mesh is inadequate and the problem requires finer meshes.

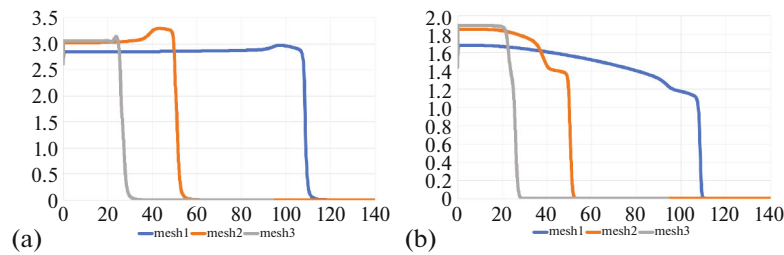


Fig. 16. Maximal velocity [mm s⁻¹] (a), density normalized kinetic energy $\frac{1}{2} \int_{\Omega} |\mathbf{u}|^2 dx$ [mm⁵ s⁻²] (b).

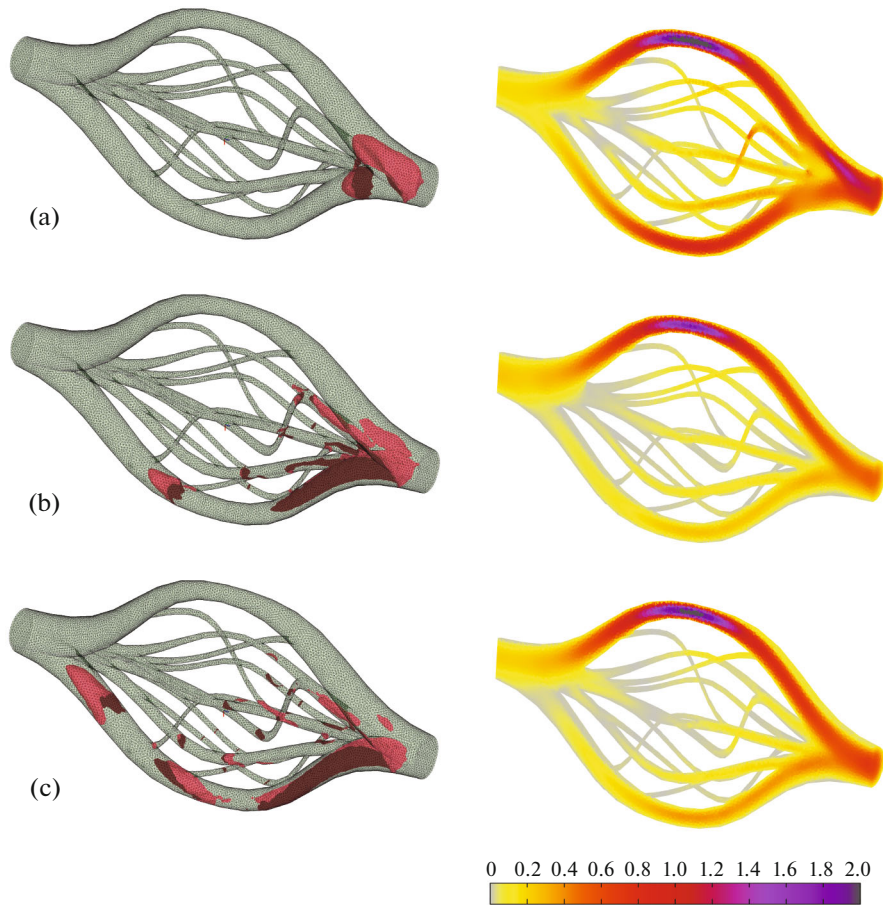


Fig. 17. Clot isosurface $\varphi = 0$ (left) and velocity magnitude (right) at the (a) beginning of time period $t = 0$ s, (b) middle of time period $t = 50$ s, (c) end of time period $t = 100$ s. Pink and brown colors correspond to outer and inner (with respect to the clot) sides of the isosurface. Part of clot boundary touching vessels boundary is not shown.

The linear systems generated for this problem are named in the followup paper [17] by **Bfs1**, **Bfs2**, and **Bfs3** for the coarse, finer, and finest meshes, respectively.

5.3. Simulations in the Simplified Capillary Network

We solve numerically the Navier–Stokes–Cahn–Hilliard equations (3) in the simplified capillary network for the time period $t \in [0, 100]$ s with time step $\Delta t = 0.025$. The inflow pressure $p = 2000 \text{ mm}^2 \text{ s}^{-2}$ is set at the boundary part $\partial\Omega|_{z=-8}$, and zero outflow pressure is set at $\partial\Omega|_{z=8}$, the no-slip condition is set at the rest of the domain boundary. The clot is set by the initial value of $\varphi = \text{sgn} \left(0.5 - \sqrt{(x-4)^2 + y^2 + (z-7)^2} \right)$. The isosurface $\varphi = 0$ for the clot and the magnitude of

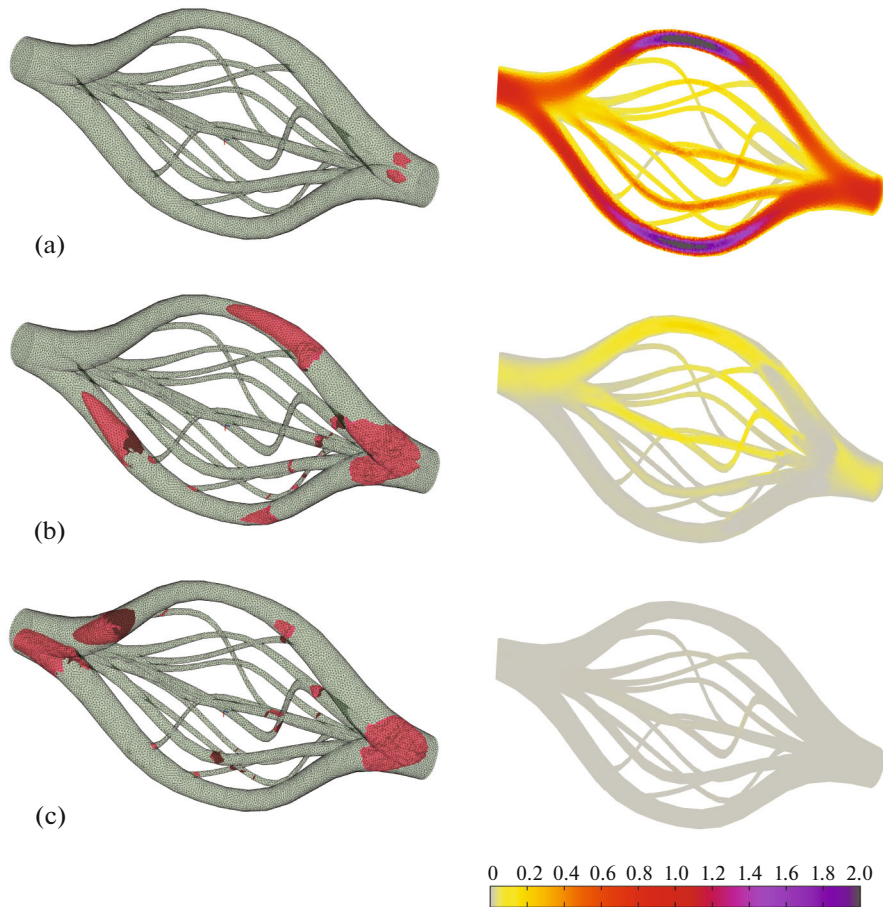


Fig. 18. Permeability isosurface $\nu_b/K = 40 \text{ s}^{-1}$ (left) and velocity magnitude $[\text{mm s}^{-1}]$ (right) at the (a) beginning of time period $t = 0 \text{ s}$, (b) middle of time period $t = 22.5 \text{ s}$, (c) end of time period $t = 45 \text{ s}$. Pink and brown colors correspond to outer and inner (with respect to the clot) sides of the isosurface. Part of clot boundary touching vessels boundary is not shown.

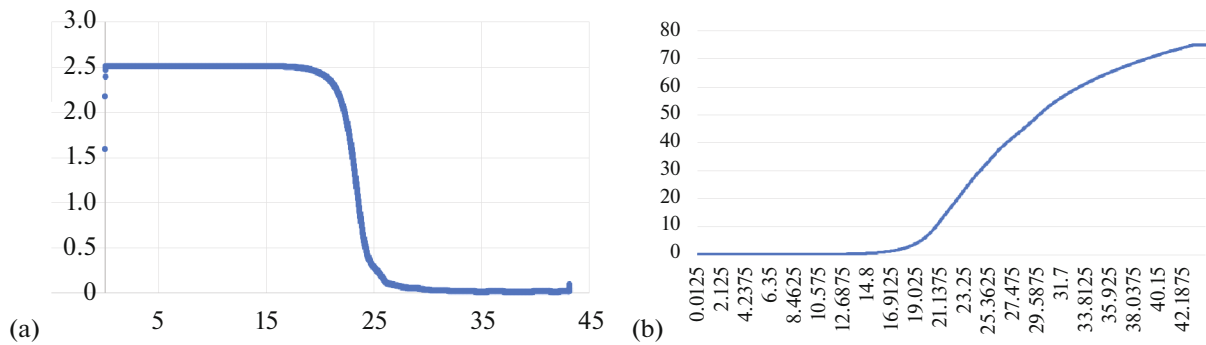


Fig. 19. Velocity magnitude (a) and volumetric occlusion in % (b).

the blood flow velocity throughout the simulation are demonstrated in Fig. 17. The clot is smeared along the walls of some vessels and eventually occludes the bottom vessel, resulting in rearrangement of the blood flow.

The linear systems generated for this problem are named in the followup paper [17] by **Bcnm**.

We solve the Navier–Stokes–Brinkman problem with coagulation chemical kinetics (4) in the simplified capillary network domain for the time period $t \in [0, 45] \text{ s}$ with time step $\Delta t = 0.0125$. The domain does not move in this case. The damaged endothelium is defined at the part of the boundary $\partial\Omega$

satisfying $\sqrt{(x-4)^2 + (y-0.6)^2 + (z-7)^2} < 0.5$. The evolution of the clot growth is demonstrated in Fig. 18. The reduction of maximal velocity and the growth of the occlusion rate in Fig. 19 indicate that the complete embolization occurs at $t = 25$ s.

The linear systems generated for this problem are named in the followup paper [17] by **Bcns**.

6. CONCLUSIONS

The present paper is the first paper in the series devoted to supercomputing of multiphysical problems of blood flow and coagulation. We have considered three mathematical models in moving and static domains, discretization of the coupled transient partial differential equations and simulation results in three domains from clinical applications: the right ventricle, the artery bifurcation, the simplified capillary network. The model address blood flows, drifting clots in blood streams, growing clots in blood streams. The models are appealing for clinicians as they may be used for risk assessment of medical procedures. For the discretization of the differential problems, we have applied the first-order accurate in-time moving-mesh collocated finite-volume method. The results of simulations indicate that the considered multiphysics problems may be solved with acceptable accuracy on parallel clusters. All the problems are solved using 50 nodes or 700 cores of the “Lomonosov-2” supercomputer [40].

The second paper [17] of the series will address the parallel solution issues of the presented simulations: convergence of iterative solvers for systems of linear algebraic equations that appear after discretizations of the above multiphysical equations, computational work for each step of the simulation, parallel efficiency of the simulations.

The future work will be directed towards improving the time accuracy of the discretization method, as well as increasing the physics complexity: the nonlinear blood rheology and interaction with the poroelastic boundaries of the blood vessels.

ACKNOWLEDGMENTS

The research is carried out using the equipment of the shared research facilities of HPC computing resources at Lomonosov Moscow State University. We would like to thank Alexander Danilov for providing the meshes of the right ventricle.

FUNDING

This work was supported by the Ministry of Education and Science of the Russian Federation, agreement 075-15-2022-286 (problem statements) and the Russian Science Foundation (project no. 21-71-20024 (solution methods), project link <https://rscf.ru/en/project/21-71-20024/>).

CONFLICT OF INTEREST

The authors of this work declare that they have no conflicts of interest.

REFERENCES

1. M. Anand, M. A. Pantelev, and F. I. Ataullakhanov, “Computational models of hemostasis: Degrees of complexity,” *Appl. Eng. Sci.* **10**, 100103 (2022). <https://doi.org/10.1016/j.apples.2022.100103>
2. F. I. Ataullakhanov and M. A. Pantelev, “Towards virtual coagulation,” *Pathophysiol. Haemost. Thromb.* **34**, 58–59 (2005). <https://doi.org/10.1159/000089926>
3. N. Bessonov, A. Sequeira, S. Simakov, Yu. Vassilevskii, and V. Volpert, “Methods of blood flow modelling,” *Math. Model. Nat. Phenom.* **11**, 1–25 (2016). <https://doi.org/10.1051/mmnp/201611101>
4. A. Bouchnita, K. Terekhov, P. Nony, Y. Vassilevski, and V. Volpert, “A mathematical model to quantify the effects of platelet count, shear rate, and injury size on the initiation of blood coagulation under venous flow conditions,” *PloS One* **15**, e0235392 (2020). <https://doi.org/10.1371/journal.pone.0235392>
5. A. Bouchnita, V. Volpert, N. Kozulinas, A. V Belyaev, and G. Panasenکو, “Multiphase patient-specific simulations to study fibrillation-induced thrombosis in the left atrial appendage,” *Phys. Fluids* **36**, 071912 (2024). <https://doi.org/10.1063/5.0216196>

6. F. Boyer, “A theoretical and numerical model for the study of incompressible mixture flows,” *Comput. Fluids* **31**, 41–68 (2002). [https://doi.org/10.1016/S0045-7930\(00\)00031-1](https://doi.org/10.1016/S0045-7930(00)00031-1)
7. I. D. Butakov and K. M. Terekhov, “Two methods for the implicit integration of stiff reaction systems,” *Comput. Methods Appl. Math.* **23**, 83–92 (2023). <https://doi.org/10.1515/cmam-2022-0083>
8. J. M. Carson, S. Pant, C. Roobottom, R. Alcock, P. Javier Blanco, C. Alberto Bulant, Yu. Vassilevski, S. Simakov, T. Gamilov, and R. Pryamonosov, “Non-invasive coronary CT angiography-derived fractional flow reserve: A benchmark study comparing the diagnostic performance of four different computational methodologies,” *Int. J. Numer. Method. Biomed. Eng.* **35**, e3235 (2019). <https://doi.org/10.1002/cnm.3235>
9. A. A. Danilov, A. V. Lozovsky, K. M. Terekhov, and Yu. V. Vassilevsky, “Higher order numerical solution of the incompressible Navier–Stokes equations in moving domains: Finite elements vs. finite volumes,” *Comput. Math. Phys.* (2025, in press).
10. A. A. Danilov, K. M. Terekhov, and Yu. V. Vassilevsky, “Dynamic adaptive moving mesh finite volume method for Navier–Stokes equations,” *Lect. Notes Comput. Sci. Eng.* **152** (2025, in press). <https://doi.org/10.1002/cnm.3731>
11. T. Galochkina, A. Bouchnita, P. Kurbatova, and V. Volpert, “Reaction–diffusion waves of blood coagulation,” *Math. Biosci.* **288**, 130–139 (2017). <https://doi.org/10.1016/j.mbs.2017.03.008>
12. T. M. Gamilov, P. Yu. Kopylov, R. A. Pryamonosov, and S. S. Simakov, “Virtual fractional flow reserve assessment in patient-specific coronary networks by 1D hemodynamic model,” *Russ. J. Numer. Anal. Math. Model.* **30**, 269–276 (2015). <https://doi.org/10.1515/rnam-2015-0024>
13. D. Han and X. Wang, “A second order in time, uniquely solvable, unconditionally stable numerical scheme for Cahn–Hilliard–Navier–Stokes equation,” *J. Comput. Phys.* **290**, 139–156 (2015). <https://doi.org/10.1016/j.jcp.2015.02.046>
14. H. C. Hemker and F. I. Ataullakhanov, “Good mathematical practice: Simulation of the hemostatic-thrombotic mechanism, a powerful tool but one that must be used with circumspection,” *Pathophysiol. Haemost. Thromb.* **34**, 55–57 (2005). <https://doi.org/10.1159/000089925>
15. M. F. Hockin, K. C. Jones, S. J. Everse, and K. G. Mann, “A model for the stoichiometric regulation of blood coagulation,” *J. Biol. Chem.* **277**, 18322–18333 (2002). <https://doi.org/10.1074/jbc.M201173200>
16. V. J. Katz, “The history of Stokes’ theorem,” *Math. Mag.* **52**, 146–156 (1979).
17. I. Konshin, K. Terekhov, and Y. Vassilevski, “Solving coupled problems of blood flow and coagulation in moving domains, II: Algebraic solvers and their parallel performance,” *Lobachevskii J. Math.* **46** (1) (2025, in press).
18. A. L. Kuharsky and A. L. Fogelson, “Surface-mediated control of blood coagulation: The role of binding site densities and platelet deposition,” *Biophys. J.* **80**, 1050–1074 (2001). [https://doi.org/10.1016/S0006-3495\(01\)76085-7](https://doi.org/10.1016/S0006-3495(01)76085-7)
19. K. Leiderman and A. L. Fogelson, “Grow with the flow: A spatial–temporal model of platelet deposition and blood coagulation under flow,” *Math. Med. Biol.: J. IMA* **28**, 47–84 (2011). <https://doi.org/10.1093/imammb/dqq005>
20. S. Minjeaud, “An unconditionally stable uncoupled scheme for a triphasic Cahn–Hilliard/Navier–Stokes model,” *Numer. Methods Part. Differ. Equat.* **29**, 584–618 (2013). <https://doi.org/10.1002/num.21721>
21. Q. Nie, Y.-T. Zhang, and R. Zhao, “Efficient semi-implicit schemes for stiff systems,” *J. Comput. Phys.* **214**, 521–537 (2006). <https://doi.org/10.1016/j.jcp.2005.09.030>
22. M. A. Panteleev, N. M. Ananyeva, F. I. Ataullakhanov, and E. L. Saenko, “Mathematical models of blood coagulation and platelet adhesion: Clinical applications,” *Curr. Pharm. Des.* **13**, 1457–1467 (2007). <https://doi.org/10.2174/138161207780765936>
23. A. N. Patel, R. J. Amrutiya, and B. N. Manvar, “A proposed approach for the management of clot-in-transit,” *Cureus* **14**, e28481 (2022). <https://doi.org/10.7759/cureus.28481>
24. M. Ranucci, T. Laddomada, M. Ranucci, and E. Baryshnikova, “Blood viscosity during coagulation at different shear rates,” *Physiol. Rep.* **2**, e12065 (2014). <https://doi.org/10.14814/phy2.12065>
25. G. Romero, M. L. Martinez, J. Maroto, and J. Felez, “Blood clot simulation model by using the bond–graph technique,” *Sci. World J.* **2013**, 519047 (2013). <https://doi.org/10.1155/2013/519047>
26. Y. Seo, H. Maeda, T. Ishizu, T. Ishimitsu, S. Watanabe, K. Aonuma, and I. Yamaguchi, “Peak C-reactive protein concentration correlates with left ventricular thrombus formation diagnosed by contrast echocardiographic left ventricular opacification in patients with a first anterior acute myocardial infarction,” *Circ. J.* **70**, 1290–1296 (2006). <https://doi.org/10.1253/circj.70.1290>
27. K. Terekhov, “Parallel multilevel linear solver within INMOST platform,” in *Supercomputing, Proceedings of the 6th Conference Russian Supercomputing Days, RuSCDays 2020*, Moscow, Russia, September 21–22, 2020, Rev. Sel. Papers 6 (Springer, 2020), pp. 297–309. https://doi.org/10.1007/978-3-030-64616-5_26

28. K. M. Terekhov, “Collocated finite-volume method for the incompressible Navier–Stokes problem,” *J. Numer. Math.* **29**, 63–79 (2021). <https://doi.org/10.1515/jnma-2020-0008>
29. K. M. Terekhov, “Fully-implicit collocated finite-volume method for the unsteady incompressible Navier–Stokes problem,” in *Numerical Geometry, Grid Generation and Scientific Computing: Proceedings of the 10th International Conference, NUMGRID 2020/Delaunay 130, Celebrating the 130th Anniversary of Boris Delaunay, Moscow, Russia, November 2020* (Springer, 2021), pp. 361–374. https://doi.org/10.1007/978-3-030-76798-3_23
30. K. M. Terekhov, “General finite-volume framework for saddle-point problems of various physics,” *Russ. J. Numer. Anal. Math. Model.* **36**, 359–379 (2021). <https://doi.org/10.1515/rnam-2021-0029>
31. K. M. Terekhov, “Pressure boundary conditions in the collocated finite-volume method for the steady Navier–Stokes equations,” *Comput. Math. Math. Phys.* **62**, 1345–1355 (2022). <https://doi.org/10.1134/S0965542522080139>
32. K. M. Terekhov, I. D. Butakov, A. A. Danilov, and Yu. V. Vassilevski, “Dynamic adaptive moving mesh finite-volume method for the blood flow and coagulation modeling,” *Int. J. Numer. Method. Biomed. Eng.* **39**, e3731 (2023). <https://doi.org/10.1002/cnm.3731>
33. K. M. Terekhov and Yu. V. Vassilevski, “Finite volume method for coupled subsurface flow problems, II: Poroelasticity,” *J. Comput. Phys.* **462**, 111225 (2022). <https://doi.org/10.1016/j.jcp.2022.111225>
34. N. Tobin, M. Li, G. Hiller, A. Azimi, and K. B. Manning, “Clot embolization studies and computational framework for embolization in a canonical tube model,” *Sci. Rep.* **13**, 14682 (2023). <https://doi.org/10.1038/s41598-023-41825-8>
35. M. Tsiang, L. R. Paborsky, W.-X. Li, A. K. Jain, C. T. Mao, K. E. Dunn, D. W. Lee, S. Y. Matsumura, M. D. Matteucci, S. E. Coutre, et al., “Protein engineering thrombin for optimal specificity and potency of anticoagulant activity in vivo,” *Biochemistry* **35**, 16449–16457 (1996). <https://doi.org/10.1021/bi9616108>
36. Y. Vassilevski, A. Danilov, A. Lozovskiy, M. Olshanskii, V. Salamatova, S. M. Chang, Y. Han, and C. H. Lin, “A stable method for 4D CT-based CFD simulation in the right ventricle of a TGA patient,” *Russ. J. Numer. Anal. Math. Model.* **35**, 315–324 (2020). <https://doi.org/10.1515/rnam-2020-0026>
37. Y. Vassilevski, M. Olshanskii, S. Simakov, A. Kolobov, and A. Danilov, *Personalized Computational Hemodynamics: Models, Methods, and Applications for Vascular Surgery and Antitumor Therapy* (Academic, New York, 2020). <https://doi.org/10.1016/C2017-0-02421-7>
38. Yu. Vassilevski, K. Terekhov, K. Nikitin, and I. Kapyrin, *Parallel Finite Volume Computation on General Meshes* (Springer, Cham, 2020). <https://doi.org/10.1007/978-3-030-47232-0>
39. Yu. V. Vassilevski, K. A. Beklemysheva, G. K. Grigoriev, A. O. Kazakov, N. S. Kulberg, I. B. Petrov, V. Yu. Salamatova, and A. V. Vasyukov, “Transcranial ultrasound of cerebral vessels in silico: Proof of concept,” *Russ. J. Numer. Anal. Math. Model.* **31**, 317–328 (2016). <https://doi.org/10.1515/rnam-2016-0030>
40. Vl. V. Voevodin, A. S. Antonov, D. A. Nikitenko, P. A. Shvets, S. I. Sobolev, I. Yu. Sidorov, K. S. Stefanov, Vad. V. Voevodin, and S. A. Zhumatiy, “Supercomputer Lomonosov-2: Large scale, deep monitoring and fine analytics for the user community,” *Supercomput. Front. Innov.* **6** (2), 4–11 (2019). <https://doi.org/10.14529/jsfi190201>
41. E. M. Wiebe, A. R. Stafford, J. C. Fredenburgh, and J. I. Weitz, “Mechanism of catalysis of inhibition of factor IXa by antithrombin in the presence of heparin or pentasaccharide,” *J. Biol. Chem.* **278**, 35767–35774 (2003). <https://doi.org/10.1074/jbc.M304803200>
42. R. P. Woodard, “The theorem of Ostrogradsky,” arXiv: 1506.02210 (2015). <https://doi.org/10.48550/arXiv.1506.02210>
43. Q. Wu, Y. Vassilevski, S. Simakov, and F. Liang, “Comparison of algorithms for estimating blood flow velocities in cerebral arteries based on the transport information of contrast agent: An in silico study,” *Comput. Biol. Med.* **141**, 105040 (2022). <https://doi.org/10.1016/j.compbiomed.2021.105040>
44. W.-T. Wu, M. A. Jamiolkowski, W. R. Wagner, N. Aubry, M. Massoudi, and J. F. Antaki, “Multi-constituent simulation of thrombus deposition,” *Sci. Rep.* **7**, 42720 (2017). <https://doi.org/10.1038/srep42720>
45. A. R. Wufsus, N. E. Macera, and K. B. Neeves, “The hydraulic permeability of blood clots as a function of fibrin and platelet density,” *Biophys. J.* **104**, 1812–1823 (2013). <https://doi.org/10.1016/j.bpj.2013.02.055>

Publisher’s Note. Pleiades Publishing remains neutral with regard to jurisdictional claims in published maps and institutional affiliations.

AI tools may have been used in the translation or editing of this article.